

Lattice-dynamical calculations for Chevrel-phase superconductors

S. D. Bader and S. K. Sinha

Argonne National Laboratory, Argonne, Illinois 60439

(Received 8 May 1978)

Born-von Kármán (BvK) lattice-dynamical calculations were performed for the rhombohedral Chevrel-phase superconductors such as PbMo_6S_8 . The dynamical matrix was obtained using Lennard-Jones (LJ) potentials, which describe interactions between Mo-Mo, Mo-S, S-S, and Pb-S pairs of atoms. The parameters for these potentials were adjusted using the comparison of the moments of the phonon spectrum $F(\omega)$ with their values obtained from heat-capacity data. Dispersion curves along the threefold axis show a splitting of the three Pb-atom-dominated modes into a low-lying transverse doublet and a longitudinal singlet. These branches hybridize with the acoustic branches. $F(\omega)$ is calculated for binary and ternary Chevrel-phase sulfides and selenides by making appropriate mass changes. Moments and site-dependent projections of $F(\omega)$ are calculated and their associated Debye temperatures are tabulated. Torsional character is found for certain modes in agreement with previous identifications made using the molecular-crystal model. The heat capacity, entropy, inelastic neutron-scattering spectra, Mössbauer recoil-free fraction for ^{119}Sn , anharmonicity, the apparent T^2 resistivity below 40 K for sputtered films, and the form of the superconducting tunneling spectrum α^2F are discussed. The applicability of the BvK approach using LJ potentials indicates that short-range interactions are important. Hence, the previously introduced molecular-crystal model is a reasonable, though not rigorous, simplification of the lattice dynamics of this important class of superconductors.

I. INTRODUCTION

The ternary compounds of the form $X\text{Mo}_6\text{S}_8$ or $X\text{Mo}_6\text{Se}_8$ which form the Chevrel-phase¹ structure are a highly interesting group of materials which have received considerable attention in the last few years.²⁻⁸ In these materials the X site can be occupied by any one of a large class of metal atoms⁹ ranging from Cu, Fe, Pb, Sn, . . . to the rare-earth metals.¹⁰ Also, Mo_6Se_8 is known¹¹ to form the same crystal structure, with the X site being unoccupied. Some of the properties of interest of this group of materials are their generally high superconducting transition temperatures T_c ,¹² high critical fields,^{3,4,13} and in the case where X is a rare-earth metal, an apparent occurrence of both magnetic ordering and superconductivity as the temperature is lowered either consecutively or simultaneously.¹⁴⁻¹⁶

There has been progress recently in understanding the electronic band structure of these compounds,^{17,18} but a rigorous microscopic theory of the electron-phonon interaction in these materials is very hard to achieve at the present time. In this work, we have constructed a phenomenological model of the lattice dynamics of this group of compounds, in an attempt to elucidate the basic structure of the phonon spectrum in a manner consistent with recent heat-capacity,^{7,19,20} neutron scattering,^{5,6,20} and Mössbauer^{21,22} measurements. In addition, such a model might prove useful as a basis for a microscopic understanding of the superconducting properties of these ma-

terials.

Figure 1 shows schematically the crystal structure of the Chevrel-phase compounds.⁹ It consists basically of Mo_6S_8 or Mo_6Se_8 octahedra as the basic units arranged in a quasicubic structure (with a rhombohedral distortion), with the X site occupying the interstitial sites of the rhombohedral lattice. The lattice constants and rhombohedral angles for the various compounds appear in Ref. 1. The X atom occupies a relatively large volume between the octahedra and its nearest neighbors are the S or Se atoms on the corners of the octahedra adjacent to the X site. Physically, this implies rather weak coupling or overlap between the electrons associated with orbitals localized on the X atom and the bonding electrons of the Mo and S (Se) atoms. In particular, if one associated the superconductivity as being primarily associated with the d electrons on the Mo atoms, it is possible to understand qualitatively why rare-earth f electron spins on the X sites are not catastrophic from the point of view of destroying Cooper pairs in the superconducting phase. An additional feature which has been observed in CuMo_6S_8 (Ref. 23) is that for this compound at least, the Cu atom sits not at the X site but on any one of six possible sites arranged in a ring about the X site, with frequent jumping between such sites. Similar phenomena have been observed in other cases when X is from the third row of the Periodic Table.²³ Quite frequently it is also observed^{1,24} that these compounds do not form stoichiometrically but with an excess of

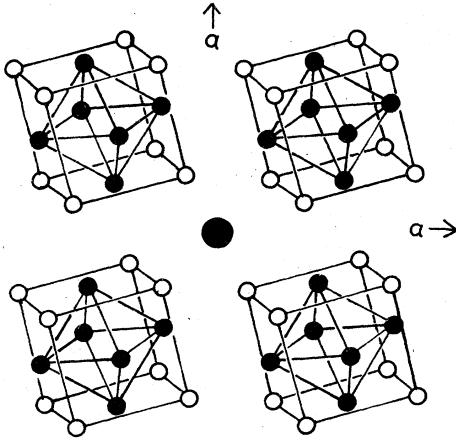


FIG. 1. Illustration of the crystal structure of Chevrel-phase compounds (after Ref. 9). Four Mo_6S_8 (or Mo_6Se_8) units are shown occupying the four front corners and an X atom (large solid circle) the body-centered position of an imagined cube. Rhombohedral directions are indicated by arrows.

about 20% of X atoms. The results²³ for CuMo_6S_8 imply that there is enough space in the region around the X site to accommodate occasionally more than a single X atom on these sites. Two conclusions may be drawn from this. One is that the potential experienced by the X atom is not likely to be a deep quasiharmonic-type potential well, but may have subsidiary minima around the central minimum, or at least be relatively anharmonic. The second is that quite often a situation exists in which two X atoms may be sitting around an X site as an interstitial dumb-bell pair, with consequent effects on the lattice dynamics in terms of resonant modes, etc. While these are important effects which undoubtedly have to be investigated further, we have in the present work restricted ourselves to the purely stoichiometric compounds and worked in the harmonic approximation in order to provide a basis on which further refinements such as the above can be made. We note that the Argonne neutron scattering measurements^{6,20} with which the present calculations are compared were performed on PbMo_6S_8 and SnMo_6S_8 samples which were actually stoichiometric.

In interpreting the heat-capacity^{7,19,20} and neutron scattering data,^{5,6,20} use was made of a molecular-crystal model which arises naturally from a consideration of the crystal structure (Fig. 1). In this model, we decompose the lattice dynamics into external and internal modes of the octahedra, the external modes being associated with torsional oscillations of the octahedra and with translational degrees of freedom of these

octahedra coupled to the translational degrees of freedom of the X atoms as in a crystal with two atoms per cell. In this model, couplings between these different modes are neglected. We discuss later the validity of this model in view of the present calculations.

II. DESCRIPTION OF THE CALCULATION

A standard Born-von Kármán (BvK) approach was used, rather than the molecular-crystal formulation of the lattice dynamics. By using a BvK approach all degrees of freedom are treated together, hence couplings between internal and external modes are automatically taken into account. The vibrational frequencies $\omega_j(\vec{q})$, where j denotes a branch index ($j=1, \dots, 3n$), and n is the number of atoms in the unit cell, are obtained by solving the secular equations

$$|D_{\alpha\beta}^{\kappa\kappa'}(\vec{q}) - \omega_j^2(\vec{q})\delta_{\alpha\beta}\delta_{\kappa\kappa'}| = 0. \quad (1)$$

$D(\vec{q})$, the dynamical matrix at wave vector \vec{q} , is a $3n \times 3n$ matrix whose elements $D_{\alpha\beta}^{\kappa\kappa'}$ were evaluated using the expression

$$D_{\alpha\beta}^{\kappa\kappa'}(\vec{q}) = \frac{1}{\sqrt{M_\kappa M_{\kappa'}}} \left(\sum_l \phi_{\alpha\beta}^{\kappa\kappa'}(0l) e^{i\vec{q}\cdot\vec{r}_l} \right) - \delta_{\kappa\kappa'} \sum_{l'',\kappa''} \phi_{\alpha\beta}^{\kappa\kappa''}(0l''), \quad (2)$$

where M_κ is the mass of the κ th atom in the unit cell and \vec{r}_l is the vector from the origin to the unit cell l . The force constant $\phi_{\alpha\beta}^{\kappa\kappa'}(0l)$ is the negative of the force exerted in the α direction on atom κ located in unit cell $l=0$ at the origin, due to a unit displacement in the β direction of atom κ' in the l th unit cell. The interactions between atoms were taken to be of the pair-potential form, and the force constants were evaluated using the following

$$\begin{aligned} \phi_{\alpha\beta}^{\kappa\kappa'}(0l) &= - \left(\frac{\partial^2 V^{\kappa\kappa'}(r)}{\partial r_\alpha \partial r_\beta} \right)_{\vec{r} = \vec{r}_l + \vec{r}_{\kappa'} - \vec{r}_\kappa} \\ &= X\delta_{\alpha\beta} + Y \frac{r_\alpha r_\beta}{r^2}, \end{aligned}$$

where

$$\begin{aligned} r_\alpha &= (\vec{r}_l + \vec{r}_{\kappa'} - \vec{r}_\kappa)_\alpha, \\ r &= |\vec{r}_l + \vec{r}_{\kappa'} - \vec{r}_\kappa|, \\ X &= V''^{\kappa\kappa'}(r)/r, \end{aligned}$$

and

$$Y = V'''^{\kappa\kappa'}(r) - V''^{\kappa\kappa'}(r)/r.$$

The potentials $V^{\kappa\kappa'}(r)$ were taken to be of the

TABLE I. Lennard-Jones parameters used in lattice-dynamical calculations.

$\kappa\kappa'$	$A^{\kappa\kappa'}$ (erg)	$\sigma^{\kappa\kappa'}$ (Å)
Mo-Mo	3.9×10^{-12}	2.4
S-S	1.8×10^{-13}	3.7
Mo-S	2.0×10^{-12}	2.2
Pb-S	2.15×10^{-12}	2.65

Lennard-Jones (LJ) form:

$$V^{\kappa\kappa'}(r) = A^{\kappa\kappa'} \left[\left(\frac{r}{\sigma^{\kappa\kappa'}} \right)^{-12} - \left(\frac{r}{\sigma^{\kappa\kappa'}} \right)^{-6} \right],$$

where $A^{\kappa\kappa'}$ and $\sigma^{\kappa\kappa'}$ were adjustable parameters. $V^{\kappa\kappa'}(r)$ and $V''^{\kappa\kappa'}(r)$ denote the first and second derivatives of $V^{\kappa\kappa'}(r)$, respectively. Four different potentials were used for $V^{\kappa\kappa'}(r)$ for PbMo_6S_8 , which describe interactions between two Mo atoms, two S atoms, an Mo atom and a S atom, and a Pb atom and a S atom. These potentials are denoted $V^{\text{Mo-Mo}}$, $V^{\text{S-S}}$, $V^{\text{Mo-S}}$ and $V^{\text{Pb-S}}$. Associated with these four potentials are eight parameters whose values are tabulated in Table I. The eight parameters were initially guessed using the intuitive expectation that the $\sigma^{\kappa\kappa'}$ values are closely related to average atomic spacings and the $A^{\kappa\kappa'}$ values are of the order of k_B , the Boltzmann constant, times the melting point of related materials, such as Mo metal, α -S, MoS_2 , and PbS. The initial guess was used to calculate frequencies [Eq. (1)] at the Γ point ($\vec{q}=0$), where the three acoustical branches are at zero frequency. The remaining 42 solutions were used to compute a Debye temperature associated with the second moment of the $\vec{q}=0$ spectrum, and one associated with the geometric mean frequency ω_g , or logarithmic moment of the $\vec{q}=0$ spectrum. The moments and associated Debye temperatures are denoted as follows:

$$\langle \omega_j^2(\vec{q}=0) \rangle = \frac{1}{3n-3} \sum_{j=1}^{3n-3} [\omega_j(\vec{q}=0)]^2,$$

$$\Theta_{\vec{q}=0}(m=2) = (\hbar/k_B) \left[\frac{5}{3} \langle \omega_j^2(\vec{q}) \rangle \right]^{1/2}, \quad (3)$$

$$\omega_g(\vec{q}=0) = \left(\prod_{j=1}^{3n-3} \omega_j(\vec{q}=0) \right)^{1/(3n-3)}$$

$$\equiv \exp \left(\sum_{j=1}^{3n-3} \ln \omega_j(\vec{q}=0) \right), \quad (4)$$

and

$$\Theta_{\vec{q}=0}(m=0) = (\hbar/k_B) e^{1/3} \omega_g.$$

For the calculation, the lattice constant (6.551 Å), rhombohedral angle (89.33°), and the atomic positions were taken from the x-ray crystallogra-

phy study by Marezio *et al.*⁹ The transformation matrix from rhombohedral to Cartesian coordinates was constructed from the appropriate metric tensors. The sum over l in Eq. (2) included the origin cell and one layer of adjacent cells, or $3^3=27$ cells total. (To check that 27 cells was adequate, the sum was increased to $5^3=125$ cells, or two layers surrounding the origin cell and the Debye temperatures associated with the resultant moments changed a mere 0.02%.) Note also that the second sum on the right-hand side in Eq. (2) is for the evaluation of self-terms of the form $\phi_{\alpha\beta}^{\kappa\kappa}(00)$. The sum rule that requires that at equilibrium the net force is zero, indicates that $\phi_{\alpha\beta}^{\kappa\kappa}(00)$ is the negative of the sum of the forces acting at site κ in cell $l=0$ from interactions with all other atoms.

The calculated values of $\Theta_{\vec{q}=0}(m)$ for $m=0$ and 2 were compared to values reported in the literature for $\Theta(m)$ obtained from an analysis of the high-temperature heat capacity of $\text{PbMo}_{5.1}\text{S}_6$.^{7,19,20} The heat capacity $\Theta(m)$ of course is not limited to $\vec{q}=0$, so a small correction was introduced to eliminate the effect of the acoustic branches on $\Theta(m)$ obtained from the heat capacity. Otherwise, for the present purposes the phonon branches were expected to be quite nondispersive and such a comparison is not unreasonable, as will be shown. The eight parameters were then adjusted and the calculation iterated until reasonable agreement was obtained with the heat-capacity values. The final parameters for $A^{\kappa\kappa}$ were within a factor of 5 on the average of the initial guesses, while the values of $\sigma^{\kappa\kappa}$ were within 8% on the average of the initially guessed values.

III. RESULTS AND DISCUSSION

A. Dispersion curves

Dispersion curves were examined along the high-symmetry threefold axis Λ , using the values of the parameters in Table I, which were obtained above from the $\vec{q}=0$ comparison with heat-capacity results. For clarity and insight results for computer-simulated binary Mo_6S_8 also were obtained by setting the $A^{\text{Pb-S}}$ parameter of Table I equal to zero (see Fig. 2). The longitudinal-acoustic (LA) branch is a singlet, while the transverse-acoustic (TA) branch is a doublet in Fig. 2. The dispersion curves of Fig. 2 are quite ordinary in shape and it is important to note that they cut off in the 10-meV region. An acoustical cutoff frequency of ~ 10 meV was identified previously in the inelastic-neutron-scattering (INS) determination of the phonon density of states of polycrystalline PbMo_6S_8 , utilizing the molecular-crystal model.⁶ This agreement with experiment

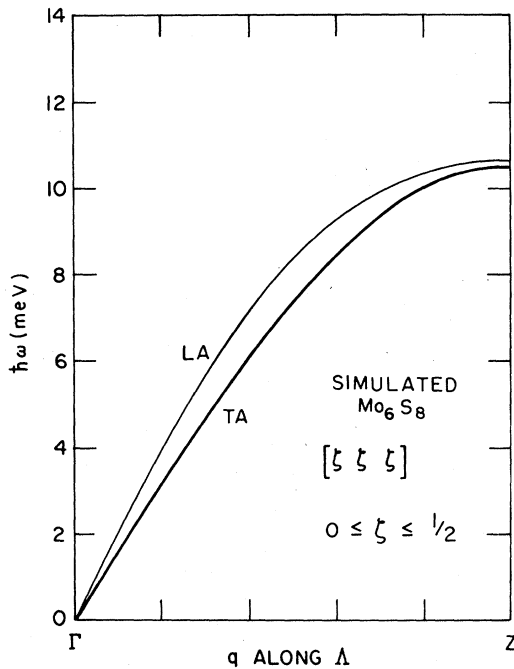


FIG. 2. Acoustical-branch dispersion curves calculated along the threefold axis for computer-simulated Mo_6S_8 . LA and TA denote the longitudinal-acoustic singlet and the transverse-acoustic doublet, respectively.

provides confidence in the reasonableness of the parameter values in Table I. $A^{\text{Pb-S}}$ was then restored to its original value and Fig. 3 shows for the ternary the three acoustical branches and three optical branches that at $\vec{q}=0$ are associated primarily with Pb-atom displacements. The acoustical branches of this ternary do not possess the simple shape found in Fig. 2 for the binary. However, it is quite clear that the unusual shape of the acoustical branches of the ternary is associated with hybridization of these branches with those of the Pb-atom-dominated optical modes. The TA doublet is repelled by the transverse-optic (TO) doublet due to symmetry-dictated non-crossing rules. The eigenvectors indicate that while displacements of the Pb atom dominate the TO branch near Γ , they dominate the TA branch near the point Z. The Pb-atom displacements are always large in the 5-meV region between Γ and Z. Hence, the experimental identification via INS^{5,6,20} that the Einstein-like feature at ~ 5 meV is due to displacements of the Pb atom is confirmed and clarified via the present calculations.

In Fig. 3 it can also be seen that the LA and LO branches repel, and in a manner often seen for molecular crystals. The dip in the LA branch near $(\frac{1}{3}, \frac{1}{3}, \frac{1}{3})$, hence, is a striking feature of the

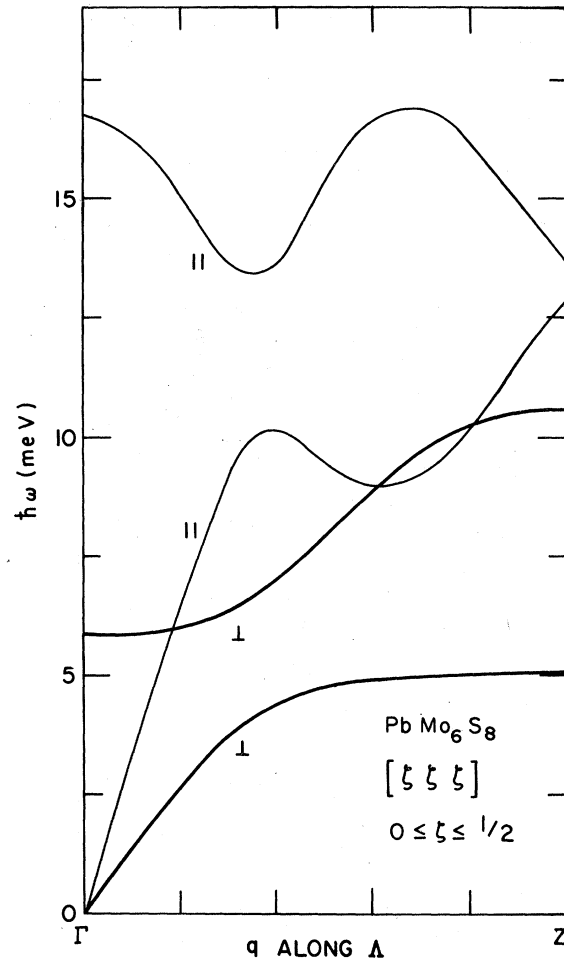


FIG. 3. Dispersion curves calculated along the threefold axis for PbMo_6S_8 showing the hybridization of the acoustical and Pb-atom-dominated optical branches. The symbols \perp and \parallel denote the transverse doublet and longitudinal singlet, respectively.

geometric arrangement for such ternary Chevrel-phase superconductors. This is in contrast to the celebrated dips in the acoustical-branch dispersion curves found experimentally²⁵ for superconductors such as Nb,²⁶ or NbC.²⁷ In these latter cases the dips have been attributed to selective phonon softening due to the \vec{q} dependence of the electron-phonon interaction²⁸ and/or peaks in $\chi(\vec{q})$, the generalized susceptibility.²⁹ We note that the dispersion curves in Fig. 3 are predictions based on our model and await experimental confirmation, which would require appropriate quality single crystals unavailable to date. In particular, it would be of interest also to see if the splitting of the TO and LO modes at $\vec{q}=0$ is as large as we obtain. Qualitatively, a splitting is expected due to the rhombohedral distortion of the sulfur cube surrounding the Pb atom. The two sulfur

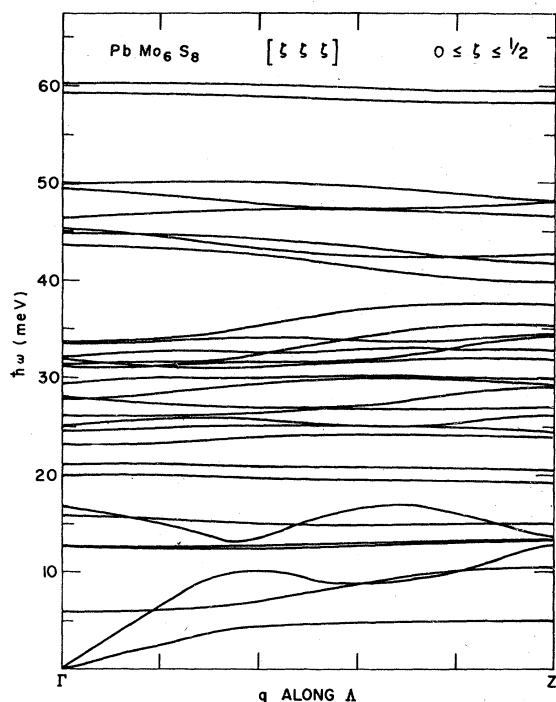


FIG. 4. Complete set of dispersion curves calculated along the threefold axis for PbMo_6S_8 .

atoms along the $[111]$ direction are closer to the Pb than the other six⁹ (2.79 vs 3.12 Å), which results in stronger bonding and a higher vibrational frequency along the $[111]$ than in the transverse direction. Figure 4 shows the dispersion curves along Λ for all 45 branches of the PbMo_6S_8 spectrum. Note the relatively dispersionless character of most of the modes.

B. Phonon density of states

The phonon density of states $F(\omega)$, where

$$F(\omega) = \sum_{\vec{q}, j} \delta(\omega - \omega_j(\vec{q})),$$

is obtained by uniformly sampling \vec{q} values over the irreducible section of the first Brillouin zone (BZ) which is $\frac{1}{12}$ the volume of the first BZ. This irreducible section was constructed from the fundamental primitive unit cell of the reciprocal lattice, rather than from the Wigner-Seitz unit cell. Only for trigonal R space groups is there no clear advantage of one method of construction over the other.³⁰ Results are shown in Fig. 5 for Mo_6Se_8 , PbMo_6S_8 , SnMo_6S_8 , and Mo_6S_8 , where the histogram bin width is 0.5 meV and 30 \vec{q} values were sampled each time. The parameter values of Table I were used for each of the four spectra in Fig. 5, except that for the binary compounds $A^{\text{Pb-S}}$ was set equal to zero, as before. Appro-

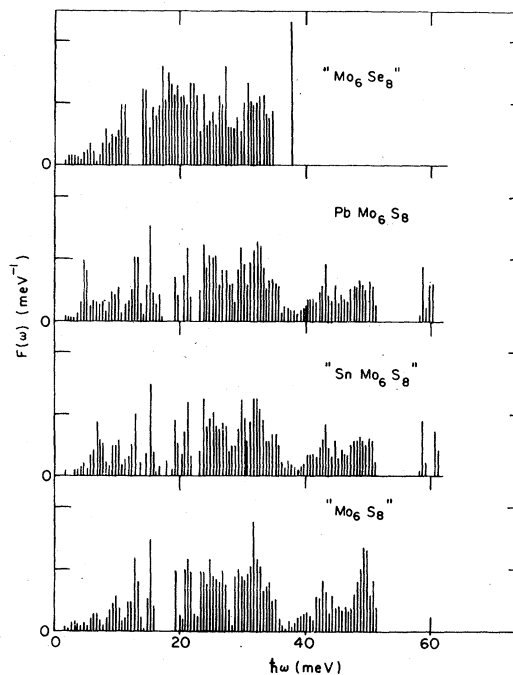


FIG. 5. $F(\omega)$ calculated for the indicated compounds. The results for the binaries and the Sn ternary were based on the parameters for PbMo_6S_8 except for appropriate mass changes and/or the switching off of the Pb-S interaction. Thirty \vec{q} values were sampled in the irreducible zone and a histogram bin width of 0.5 meV was used.

appropriate mass changes also were made to simulate $F(\omega)$ for SnMo_6S_8 and Mo_6Se_8 . The rhombohedral lattice constant and angle for PbMo_6S_8 was retained throughout. A comparison of the spectra of Mo_6Se_8 and PbMo_6S_8 indicates two clear differences that were identified in the INS experiments⁶ previously. First, the ternary sulfide has a prominent 5-meV "Einstein-like" feature, due to the Pb-atom displacements, which is absent in the binary selenide. Second, the ternary sulfide has significant spectral weight in the 40–50-meV region, while the binary selenide does not. This was correctly attributed to the mass difference between Se and S, previously.⁶ Comparison of $F(\omega)$ for SnMo_6S_8 in Fig. 5 to the INS experimental results^{5,6,20} indicates that the calculated Sn-dominated Einstein-like mode is at too high an energy (~ 7 vs ~ 5 meV), but that $A^{\text{Sn-S}} = \frac{1}{2} A^{\text{Pb-S}}$ would yield satisfactory agreement.

Convergence tests will be discussed when the moments are calculated, but it can be seen in Fig. 6 that upon increase of the number of \vec{q} values sampled to 650, the character of the spectrum for PbMo_6S_8 remains the same as found in Fig. 5. The major difference between the PbMo_6S_8 spectra of Figs. 5 and 6 is that the higher-density

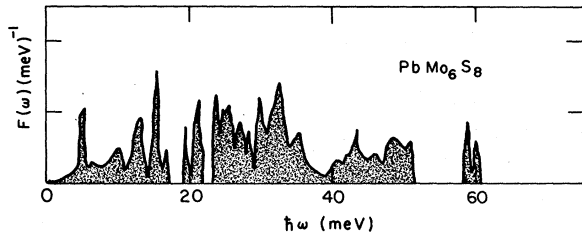


FIG. 6. $F(\omega)$ calculated for PbMo_6S_8 as in Fig. 5 except that 650 \vec{q} values were sampled in the irreducible zone. The envelope of the histogram is drawn and shaded in.

\vec{q} sampling of Fig. 6 includes enough small- \vec{q} values that the expectation that $F(\omega) = \omega^2$ as $\omega \rightarrow 0$ starts to become apparent. Also, gaps can be seen clearly in Fig. 6 straddling the 20-meV region. In the molecular-crystal model²⁰ a gap is expected in this region, which would separate the internal and external modes. (The gap just below 60 meV, however, may be an artifact of the calculation, but this need not be of concern for the present purposes).

C. Eigenvector-weighted phonon density of states

The eigenvector-weighted phonon density of states $F_i(\omega)$ uses the eigenvectors $\vec{e}_\kappa(\vec{q}, j)$ associated with atomic species i to project out of $F(\omega)$ the vibrational spectrum of i :

$$F_i(\omega) = \sum_{\vec{q}, j} \left(\sum_{\kappa} \delta_{i\kappa} \vec{e}_\kappa^*(\vec{q}, j) \cdot \vec{e}_\kappa(\vec{q}, j) \right) \delta(\omega - \omega_j(\vec{q})),$$

where

$$\vec{e}_\kappa^*(\vec{q}, j) \cdot \vec{e}_\kappa(\vec{q}, j) = \sum_{\alpha} e_{\kappa\alpha}^*(\vec{q}, j) e_{\kappa\alpha}(\vec{q}, j).$$

[The eigenvectors are contained in the matrix that diagonalized $\underline{D}(\vec{q})$ and, hence, were generated in the course of the computations.] Figure 7 shows the vibrational spectra $F_i(\omega)$ for $i = \text{Mo}, \text{S}$, and Pb individually. Each $F_i(\omega)$ was normalized to unity, so

$$F(\omega) = F_{\text{Pb}}(\omega) + 6F_{\text{Mo}}(\omega) + 8F_{\text{S}}(\omega).$$

This representation of the dynamics again shows that the low-energy Einstein-like feature is associated with the displacements of the Pb atom, while the high-energy region of the spectra is dominated by the S atomic displacements. Replacements of S for Se would remove spectral weight from the high-energy 40–50-meV region since approximately $\omega \propto M^{-1/2}$ as stated before.

D. Torsional character of mode near 12 meV

The experimental INS results⁶ exhibited a peak at ~ 12 meV which was attributed to torsional or

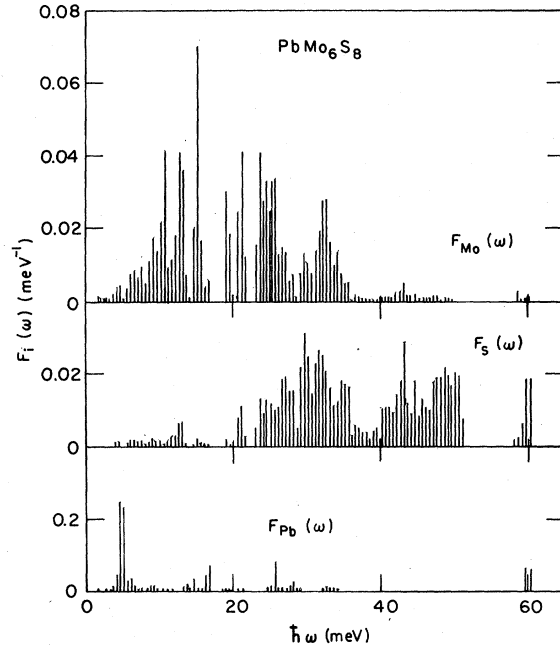


FIG. 7. $F_i(\omega)$ calculated for PbMo_6S_8 , where $i = \text{Pb}, \text{Mo},$ and S .

“rocking” motion of Mo_6S_8 quasirigid units using the molecular-crystal model. Figure 8 shows the directions of the eigenvectors associated with a Mo_6 octahedron for a $\vec{q} = 0$ mode at 12.1 meV (the sulfur atoms are not shown). The Mo atoms dominate the motion associated with this mode, while the Pb atom does not significantly participate at all. The displacements of the in-plane Mo atoms in Fig. 8 are predominantly torsional, as is schematically emphasized by the curved arrow about the axis perpendicular to the plane. However, the Mo atoms above and below the plane appear to exhibit predominantly a “breathing” motion. This type of mixed torsional-breathing mode can be understood within the molecular-crystal context as a hybridization arising from internal-external mode coupling. In an ideal mo-

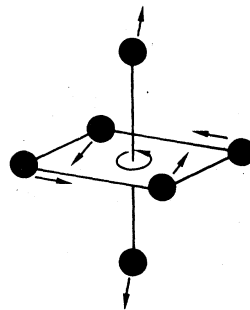


FIG. 8. Schematic of displacement vectors associated with a Mo_6 octahedron in PbMo_6S_8 for a $\vec{q} = 0$ mode at 12.1 meV. Note that the in-plane Mo atoms exhibit predominantly torsional character, as emphasized by the curved arrow about the axis, while the out-of-plane Mo atoms exhibit predominantly breathing motion. The S atoms are not shown.

lecular crystal there is an order-of-magnitude type gap between the high-energy internal modes and the low-energy external modes, and purely torsional motion can occur. As the gap closes the molecular-crystal concept breaks down. The internal and external modes interact, and purely torsional motion may give way to hybridizations such as we see in Fig. 8. From the spectra of Fig. 6 it is clear that for PbMo_6S_8 the "gaps" straddling the 20-meV region of the spectra are small and partially filled in, hence, a molecular-crystal approach cannot be rigorous. The usefulness of the molecular-crystal model is not in its rigor, but in the insight it affords. Finally, we note that torsional character in the 12-meV region was examined only at $\vec{q} = 0$ where the eigenvectors are real. For $\vec{q} \neq 0$, the eigenvectors are complex and not readily interpretable.

E. Moments and their associated Debye temperatures

Moments of $F(\omega)$ and $F_i(\omega)$ are invaluable for the evaluation of any of the standard expressions which arise in a microscopic calculation of the superconductivity properties. The second moment and zeroth or logarithmic moment already have been introduced in Sec. II [Eqs. (3) and (4)]. We write the moments and their associated Debye temperatures in integral form for $n > -3, \neq 0$:

$$\langle \omega^n \rangle = \int \omega^n F(\omega) d\omega, \quad (5)$$

$$\langle \omega^n \rangle_i = \int \omega^n F_i(\omega) d\omega, \quad (6)$$

$$\Theta_D(n) = \frac{\hbar}{k_B} \left[\left(\frac{n+3}{n} \right) \langle \omega^n \rangle \right]^{1/n}, \quad (7)$$

and

$$\Theta_i(n) = \frac{\hbar}{k_B} \left[\left(\frac{n+3}{n} \right) \langle \omega^n \rangle_i \right]^{1/n}. \quad (8)$$

The lowest moment of physical significance is for $n = -3$; its associated Debye temperature is, by definition, that obtained ultrasonically or from low-temperature heat-capacity measurements.

TABLE II. Debye temperatures associated with logarithmic and second moments of $F(\omega)$ for Chevrel-phase compounds as calculated from the model.

Compound	$\Theta_D (n=0)$ (°K)	$\Theta_D (n=2)$ (°K)
Mo_6Se_8	330	359
PbMo_6S_8	402	486
SnMo_6S_8	410	488
Mo_6S_8	428	484

TABLE III. Debye temperatures associated with n th moments of $F(\omega)$ and $F_i(\omega)$ for PbMo_6S_8 as calculated from the model.

n	$\Theta(n)$ (°K)	$\Theta_{\text{Pb}}(n)$ (°K)	$\Theta_{\text{Mo}}(n)$ (°K)	$\Theta_{\text{S}}(n)$ (°K)
-2	277	115	270	468
-1	336	110	292	531
0	402	119	318	558
1	452	142	342	573
2	486	187	364	583
3	513	248	384	593
4	553	311	403	602
5	551	367	422	610
6	566	413	441	617

Equations (5)–(8) can be used in the limit as $n \rightarrow -3$ or 0, but for $n=0$ we can also write

$$\omega_g = \exp(\langle \ln \omega \rangle) = \exp \left(\int (\ln \omega) F(\omega) d\omega \right) = \left(\prod_{j=1; \vec{q}}^{3n} \omega_j(\vec{q}) \right)^{1/3nN} \quad (9)$$

and

$$\Theta_D(0) = (\hbar/k_B) e^{1/3} \omega_g, \quad (10)$$

where N is the number of \vec{q} values sampled.

The quantities $\langle \ln \omega \rangle_i$ and $\Theta_i(0)$ are defined by Eqs. (9) and (10) if $F_i(\omega)$ is substituted for $F(\omega)$, as before. Table II contains values of $\Theta_D(2)$ and $\Theta_D(0)$ calculated from the four spectra in Fig. 5. Tables III and IV contain $\Theta_D(n)$ and $\Theta_i(n)$ for PbMo_6S_8 and Mo_6Se_8 , respectively. Figure 9 is a plot of $\Theta_i(n)$ vs n for PbMo_6S_8 . The values of $\Theta_D(2)$ and $\Theta_D(0)$ in Tables II–IV and Fig. 9 are essentially independent of whether $N=30$ or $N=650$ \vec{q} values in the irreducible zone were sampled to construct $F(\omega)$. This is because, as we have seen near the end of Sec. III B, for small- N values only the low-

TABLE IV. Debye temperatures associated with n th moments of $F(\omega)$ and $F_i(\omega)$ for Mo_6Se_8 as calculated from the model.

n	$\Theta(n)$ (°K)	$\Theta_{\text{Mo}}(n)$ (°K)	$\Theta_{\text{Se}}(n)$ (°K)
-2	266	252	277
-1	302	290	312
0	330	324	334
1	347	347	347
2	359	363	356
3	369	376	363
4	377	385	370
5	383	392	376
6	388	398	380

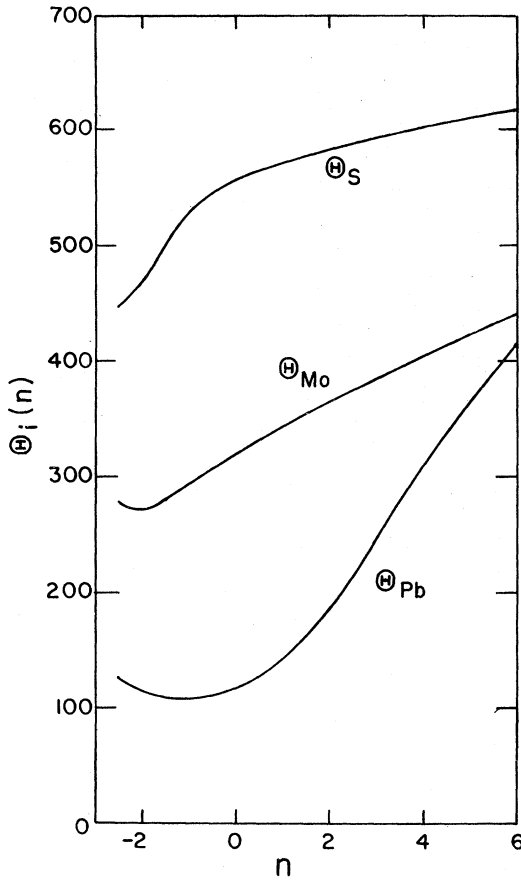


FIG. 9. Debye temperatures associated with n th moments of $F_i(\omega)$ calculated for PbMo_6S_8 .

frequency portion of the spectrum appears not to be properly characterized. Only the lower moments (i.e., as $n \rightarrow -3$) are very sensitive to the low-frequency portion of the spectrum. The higher moments (i.e., $n > 0$) become successively more sensitive to the high-frequency portion of the spectrum, and for $n=0$ each mode is weighted equally in the geometric-mean sense. Hence, convergence can be tested most sensitively by comparison of the low- n $\Theta_D(n)$ values as a function of N . We find that for $n = -1.5$, the $\Theta_D(n)$ values for $N = 30$ and 120 agree within $\sim 1\%$, but that the agreement progressively degrades to $\sim 3\%$ for $n = -2$. Hence, the $F(\omega)$ based on the 30-point sampling should be adequate, from a convergence standpoint, to describe any quantities of interest that are related to moments for which $n > -2$.

F. Lattice entropy and heat capacity

The lattice entropy S_L per gram-atom is

$$S_L(T) = 3N_A k_B \int [x n_x - \ln(n_x + 1)] F(\omega) d\omega,$$

where N_A is Avogadro's number, $x = \hbar\omega/k_B T$, n_x is the Bose-Einstein distribution function $n_x = (e^x - 1)^{-1}$, and $F(\omega)$ is normalized to unity. The heat capacity is $C_L(T) = T(dS/dT)$. The values of $C_L(T)$ and $S_L(T)$ were calculated and compared to tabular Debye C_L and S_L functions to extract $\Theta_D^C(T)$ and $\Theta_D^S(T)$, the effective Debye temperature associated with the heat capacity and entropy, respectively. The results are shown for PbMo_6S_8 in Fig. 10 and Mo_6Se_8 in Fig. 11. Experimental determinations of Θ_D^C and Θ_D^S are also shown for $\text{PbMo}_{5.1}\text{S}_6$ and SnMo_6S_8 (in Fig. 10) and Mo_6Se_8 (in Fig. 11). The agreement between the experiments and calculations is quite good. Of course, the experimental values for $\text{PbMo}_{5.1}\text{S}_6$ of Θ_D^C and Θ_D^S at high temperatures [which define $\Theta_D(n=2)$ and $\Theta_D(n=0)$, respectively] were used as constraints in the adjustment of the eight LJ parameters of Table I; so agreement at high temperatures is expected. But, note that at low temperatures the approximate position and depth of the minima in the experimental Θ curves for $\text{PbMo}_{5.1}\text{S}_6$ are reasonably approximated in the calculation. Experimental results³¹ for SnMo_6S_8 in Fig. 10 also agree quantitatively with the calculated curves. This indicates that the defect structure of the Pb-ternary sample (or, more precisely, the lack of use of stoichiometric quantities of fabricating materials) appears not to have invalidated the experimental data analysis. The good agreement between experiment and calculation may be partially fortuitous since the possible changes in force constants due to the lattice constant and rhombohedral angle changes have not been taken into account here.

G. Inelastic-neutron-scattering generalized phonon density of states

$G(\omega)$ is the weighted or generalized phonon density of states obtained in INS experiments for polycrystalline samples. $G(\omega)$ is similar to the true phonon density of states $F(\omega)$ except that there are three weighting factors:

$$G(\omega) = \sum_{\vec{q}, j} \sum_{\kappa\alpha} \left(\frac{\sigma_\kappa}{M_\kappa} \right) (e^{-2W_\kappa}) [e_{\kappa\alpha}^*(\vec{q}, j) e_{\kappa\alpha}(\vec{q}, j)] \times \delta(\omega - \omega_j(\vec{q})). \quad (11)$$

The first factor σ_κ/M_κ is the total thermal neutron scattering cross section for atom κ divided by the mass of that atom, the second is the Debye-Waller factor (DWF) e^{-2W_κ} for the atom κ , and the third is the eigenvector factor. The σ_κ/M_κ values are tabulated in Table V. The DWF can be calculated since

$$W_\kappa = \frac{1}{3} K^2 \langle u^2 \rangle_\kappa,$$

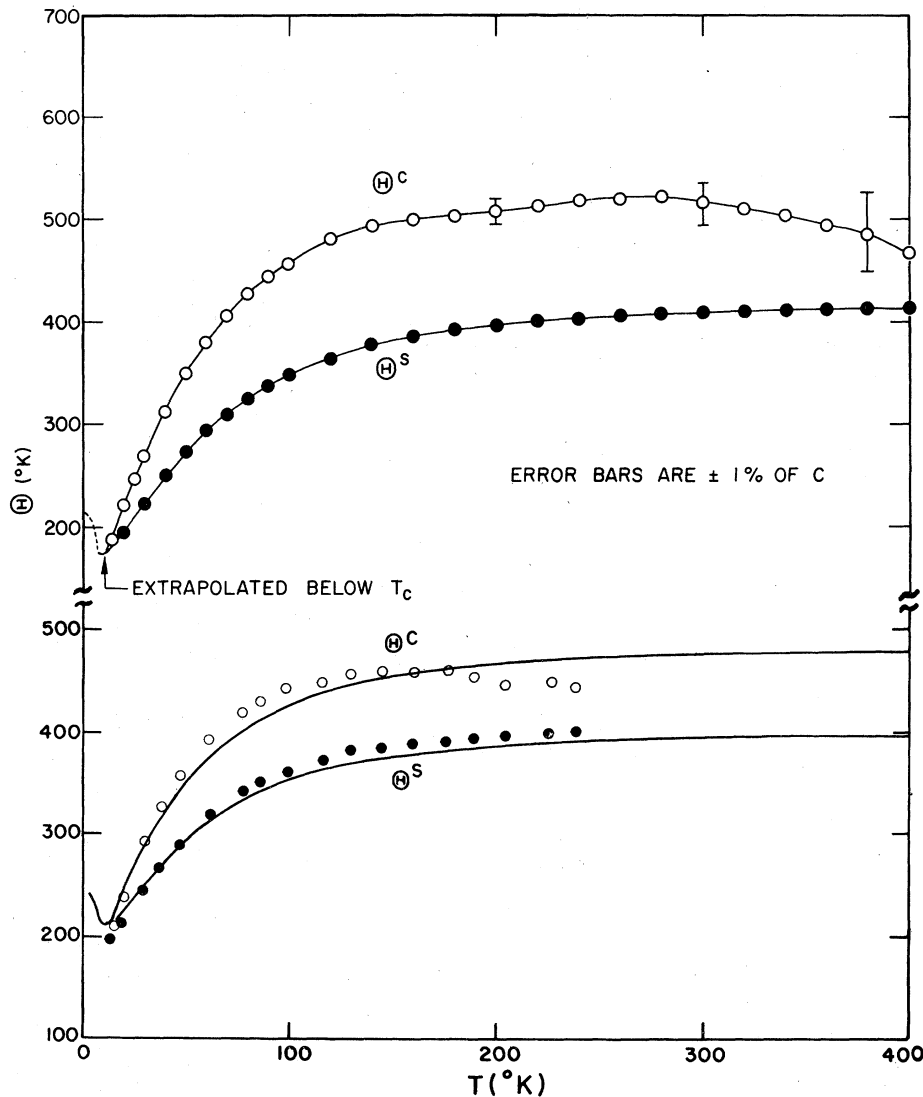


FIG. 10. Debye temperatures associated with the heat capacity (Θ^C) and entropy (Θ^S) as a function of temperature. The upper two curves drawn through the circular symbols are experimental results for PbMo_6S_8 taken from Ref. 7. The lower two curves were calculated for PbMo_6S_8 (present work). Note the similarity in shape and magnitude of the experimental results for PbMo_6S_8 and that calculated for PbMo_6S_8 . The circular symbols associated with the lower set of curves are experimental results for SnMo_6S_8 (Ref. 31). The experimental results for the stoichiometric Sn ternary are in better agreement with the calculations than those for the nonstoichiometric Pb ternary. This is because (a) the calculations assume a stoichiometric sample, and (b) on the scale plotted, the different masses of the Pb and Sn atoms do not affect a significant fraction of the frequencies which contribute at these temperatures.

where \vec{K} is the neutron momentum transfer, and $\langle u^2 \rangle_\kappa$ is the mean-square displacement of atom κ summed over the three Cartesian components α . \vec{K} depends on the initial energy E_0 , the energy gain E , and the scattering angle. For simplicity, the scattering angle was taken to be 90° in the calculation,³² while experimentally a variety of angles symmetric about 90° were also included to improve counting statistics. Hence,

$$|\vec{K}| = 0.69476(2E_0 + E)^{1/2},$$

where K is in \AA^{-1} and $E_0 = 4.83$ meV in the Argonne INS experiments.^{6,20} The mean-square displacements were calculated at $T = 300$ °K from

$$\langle u_\alpha^2 \rangle_\kappa = \frac{\hbar^2}{NM_\kappa} \sum_{\vec{q}, j} \left[\frac{1}{\hbar\omega_j(\vec{q})} \left(\frac{1}{2} + \frac{1}{\exp[\hbar\omega_j(\vec{q})/k_B T] - 1} \right) \times e_{\kappa\alpha}^*(\vec{q}, j) e_{\kappa\alpha}(\vec{q}, j) \right].$$

From these, the quantity $\langle u_x^2 \rangle_\kappa$, which corresponds to the average mean-square displacement in any particular direction, was calculated from $\langle u_x^2 \rangle_\kappa = \frac{1}{3}(\langle u_{\parallel}^2 \rangle + 2\langle u_{\perp}^2 \rangle)$, where \parallel and \perp refer to the trigonal axis (see Table VI). Each calculation of $G(\omega)$ required two cycles of diagonalizations of $D(\vec{q})$. In the first cycle the $\langle u^2 \rangle_\kappa$ values were calculated and stored, while in the second Eq. (11) was evaluated. Results for $G(\omega)$ for PbMo_6S_8 and SnMo_6S_8 are shown in Fig. 12 where 30 \vec{q} values

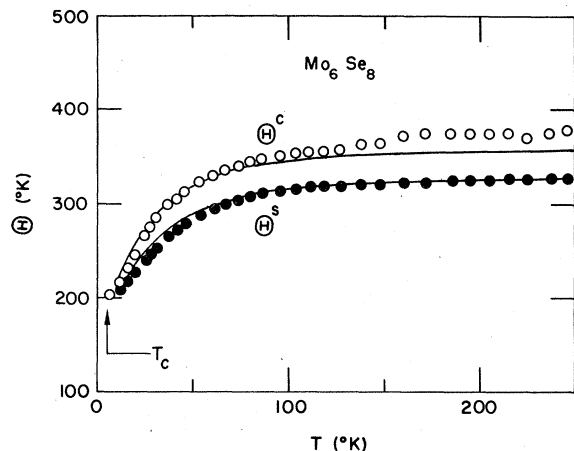


FIG. 11. Debye temperatures associated with the heat capacity (Θ^C) and entropy (Θ^S) for Mo_6Se_8 . The curves are calculated results (present work) and the circles are measured results (Ref. 31). The agreement between the calculations and experiment for Θ^C are within the 2% experimental uncertainty for the latter above 150 °K.

were sampled, the bin width is 0.5 meV and the parameters of Table I were used as in the calculation of $F(\omega)$ of Fig. 5. Comparison of Figs. 12 and 5 indicates that $G(\omega)$ is very similar to $F(\omega)$. Hence, the weighting factors do not significantly obscure the true spectrum; the INS experiments^{5,6,20} may thus be regarded as quite realistic approximations to $F(\omega)$.

The calculated $G(\omega)$ for PbMo_6S_8 is compared to the experimental⁶ $G(\omega)$ in Fig. 13, where both results are normalized to unity. This is a more stringent comparison of experiment to calculation than the heat-capacity comparison of Fig. 10, since the heat capacity averages over all the modes, while this is a mode-for-mode comparison. The difference between the spectra of Fig. 13 is partially due to the fact that the calculation used a constant 0.5-meV bin width to construct the histogram, while the experimental resolution varied from being significantly better than 0.5 meV at low energies to poorer than 0.5 meV at high energies. Nevertheless, the disagreement in the 20-meV region between the two spectra of

TABLE V. Thermal-neutron-scattering cross section to mass ratios.

κ	σ_κ/M_κ (barn/amu)
Pb	0.0560
Mo	0.0771
S	0.0375
Sn	0.0413

Fig. 13 appears to be real, and a shortcoming of the present calculations. On the whole, however, the agreement is reasonable.

H. Mössbauer effect and anharmonicity

Kimball *et al.*²¹ and Bolz *et al.*²² have measured the Mössbauer spectrum of ^{119}Sn in SnMo_6S_8 . Both these groups found anomalous behavior of the recoil-free fraction versus temperature in the sense that below ~ 100 °K this quantity did not follow a temperature dependence obtained from a harmonic phonon-spectrum calculation which was compatible with the higher-temperature data. Kimball *et al.*²¹ attributed this to large anharmonicity associated with the motion of the Sn atom, resulting in a softening of the frequencies of the modes associated with Sn displacements. Bolz *et al.*²² attributed the anomalous behavior to a softening of the librational modes of the Mo_6S_8 octahedra and to a subtle structural transformation associated with the tilt of these octahedra with respect to the unit-cell axis. The INS data²⁰ indicated that there is little softening of the frequency of the peak in $G(\omega)$ associated with the transverse Sn modes. However, we have seen that these modes are hybridized with the external modes so that a softening of the external modes (e.g., the torsional modes) could result (via a change in hybridization) in an anomalous temperature dependence of $\langle u^2 \rangle_{\text{Sn}}$. In order to investigate this further, we studied the effect on $\langle u^2 \rangle_{\text{Sn}}$ of softening all the force constants by 20% [except the Sn-S force constant which determines the Einstein-like peak in the $G(\omega)$ function]. While this does have an effect on $\langle u^2 \rangle_{\text{Sn}}$ which makes it approach more closely the observed low-temperature behavior compared with $\langle u^2 \rangle_{\text{Sn}}$ calculated from the unsoftened force constants, the effect appeared to be much too small to reproduce the actual temperature dependence of the observed recoil-free fraction.

In view of the arguments given in the Introduction regarding the anharmonic nature of the Sn atomic potential, it is likely that a quasiharmonic theory

TABLE VI. Root-mean-square displacement component $\langle u_x^2 \rangle_\kappa^{1/2}$ calculated at 300 °K.

κ	$\langle u_x^2 \rangle_\kappa^{1/2}$ (Å)
Pb	0.127
Mo ^a	0.080
S ^a	0.081

^a Value reported is average within unit cell for all atoms of this type.

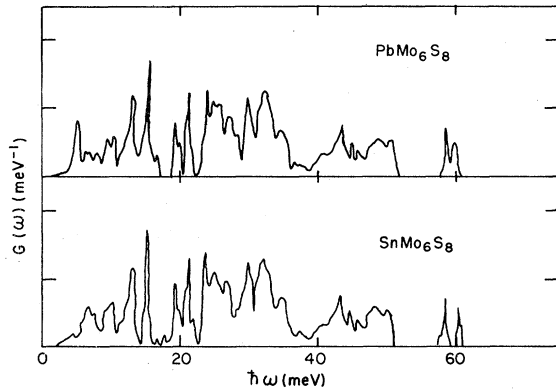


FIG. 12. $G(\omega)$ spectra calculated for PbMo_6S_8 and SnMo_6S_8 . The envelopes of the 0.5-meV bin width histograms are drawn. These $G(\omega)$ spectra are similar to the $F(\omega)$ spectra calculated in Fig. 5.

of the temperature dependence of the recoil-free fraction is not valid. Another possibility is that there is a strong temperature-dependent electron-phonon renormalization of the longitudinal-acoustic phonon modes, which would affect $\langle u^2 \rangle_{\text{Sn}}$ while leaving the position of the low-frequency peak in $G(\omega)$ (which is due predominantly to the transverse Sn modes) unchanged.

I. Resistivity and superconductivity

The temperature dependence of the electrical resistivity ρ can be calculated using the Wilson model³³ for phonon-assisted (s - d) interband scattering. In its simplest form

$$\rho(T) \propto \int \frac{y}{\sinh^2 y} \alpha_{\text{tr}}^2(\omega) F(\omega) d\omega, \quad (12)$$

where $y = \hbar\omega/2k_B T$, $\alpha_{\text{tr}}^2(\omega)$ is a transport electron-phonon coupling strength that weights $F(\omega)$, and it is assumed that the electronic density of state

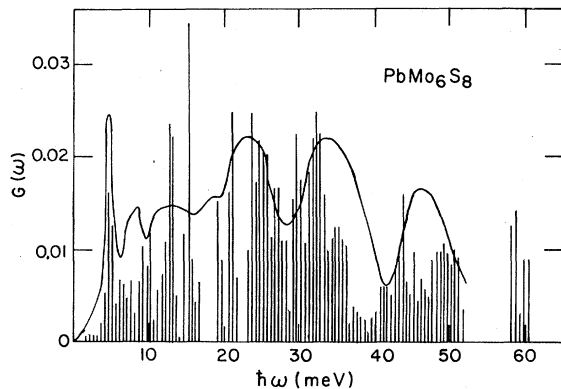


FIG. 13. $G(\omega)$ spectrum calculated for PbMo_6S_8 (histogram) as compared to the measured $G(\omega)$ spectrum taken from Ref. 6 (smooth curve).

$N(E)$ near the Fermi energy E_F is constant. Equation (12) yields the usual T^3 law as $T \rightarrow 0$, if a Debye spectrum is assumed for $F(\omega)$ and $\alpha_{\text{tr}}^2 F$. First reports of experimental findings for sputtered films of PbMo_6S_8 and the related system $\text{Cu}_z\text{Mo}_6\text{S}_8$, where $z = 1, 1.8,$ and 2.5 indicate that $\rho - \rho_0 \propto T^2$ for $T_c < T < 40$ K, where ρ_0 is a constant attributed to impurity scattering.^{34,35} This same type of unexpected T^2 behavior also is found for the classical high- T_c A-15 superconductors Nb_3Sn (Ref. 36) and V_3Si (Ref. 37), and has been explained using Eq. (12) simply by substituting a realistic $F(\omega)$ and $\alpha^2 F$ for the Debye representation more typically used.^{36,38} The idea is that T_c is outside the low-temperature limit for which the T^3 law would be observed. Figure 14 shows that this is also the case for PbMo_6S_8 . The circles plotted in Fig. 14 were calculated using Eq. (12), where α_{tr}^2 is assumed constant and the $F(\omega)$ from Fig. 5 is used for PbMo_6S_8 . The straight line drawn through the circles on the ρ vs T^2 plot indicates that the calculation recovers the temperature dependence observed experimentally for the sputtered films.^{35,36} The negative intercept of the straight line at $T^2 = 0$ indicates

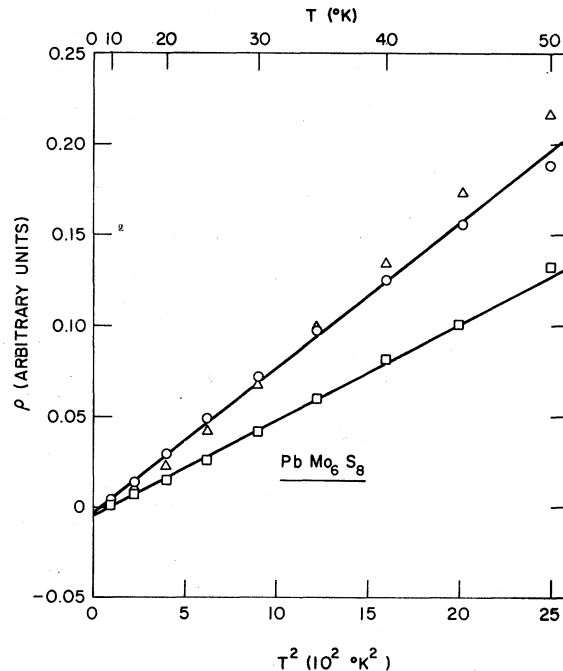


FIG. 14. Resistivity of PbMo_6S_8 plotted as ρ vs T^2 as calculated assuming $\alpha^2 F = F$ (circles), $\alpha^2 F = F - F_{\text{Pb}}$ (squares), and $\alpha^2 F = F_{\text{Mo}}$ (triangles). The straight lines that fit the first two calculations below 40 K indicate that these models for $\alpha^2 F$ are not unreasonable. The $\alpha^2 F = F_{\text{Mo}}$ model does not yield an apparent T^2 region below 40 K and, hence, can be ruled out as implausible.

that this apparent T^2 behavior is merely a limited temperature-range empirical fit and not to be regarded as signalling a "power-law"-type behavior. We mention in passing that in the high-temperature limit (i.e., $T > \Theta_D$) the simple prediction of the Wilson model [Eq. (12)] that $\rho \propto T$ is not obeyed for these ternary sulfides³⁵; instead, ρ tends to a constant "saturation" value. This type of high-temperature behavior has also been reported for $A-15$ superconductors^{37,39,40} and numerous other narrow-band metallic systems,⁴¹ and was attributed mainly to the breakdown of the assumption that $N(E)$ is constant near E_F .^{38,39} The high-temperature region, hence is beyond the scope of the simple formulation of the Wilson model [Eq. (12)] that we use, although adequate discussion of the "saturation" effect appears elsewhere.^{38-40,42} We can proceed with the lower-temperature analysis because below ~ 40 or 50 °K it is not unreasonable to assume $N(E)$ is approximately constant within a few $k_B T$ of E_F , while above Θ_D this is not necessarily the case. A second qualifying point in passing is that resistivity measurements made on compacted powders of PbMo_6S_8 yielded different results³⁵ below 40 °K than those for sputtered films, in that $\rho - \rho_0 \propto T$. This behavior is regarded as extrinsic, perhaps associated in some manner with ill-defined conduction paths within the sample, and is not treated further in this discussion.

The temperature dependence of the resistivity can be used to help determine which phonon modes are most important for superconductivity. The key is that α_{tr}^2 is very closely related to α_{sc}^2 , the superconductivity electron-phonon coupling strength.⁴³ In turn, α_{sc}^2 is used to define the electron-phonon mass enhancement λ the principle parameter of any of the T_c equations:

$$\lambda = 2 \int \frac{\alpha^2 F}{\omega} d\omega,$$

where $\alpha \equiv \alpha_{sc} \sim \alpha_{tr}$. It was shown above that if all the phonon modes are weighted equally (i.e., the α_{tr}^2 is constant assumption), that the experimental T^2 behavior is recovered below 40 °K. This might suggest that all modes contribute equally in determining λ and hence T_c . But such literal interpretations are unwarranted since $\rho(T)$ does not provide that strong a constraint on the uniqueness of $\alpha^2 F$. Instead, we ask what reasonable models can we use for α_{tr}^2 and still retain the apparent T^2 resistivity behavior below 40 °K? If a model for α_{tr}^2 does not recover the experimental $\rho(T)$ below 40 °K, then the mode weighting specified by that model clearly can be eliminated from further consideration. For instance, the argument has been made that modes

associated with Pb-atom displacements should not contribute significantly to λ , since superconductivity persists when the Pb sites contain magnetic rare-earth elements. The squares plotted in Fig. 14 were based on the assumption that $\alpha^2 F = 6F_{\text{Mo}} + 8F_{\text{S}} \equiv F - F_{\text{Pb}}$ (i.e., the Pb-atom displacements do not contribute). The straight line through the squares in Fig. 14 indicates that such a model is plausible and cannot be ruled out. This is the sense in which we believe it is appropriate to use $\rho(T)$ as a constraint on the form of $\alpha^2 F$.

The argument has been made also that the superconductivity is associated with a strong electron-phonon interaction at the Mo sites. Does this mean that S-atom displacements are not important? This is tested in Fig. 14 also. The triangles plotted were calculated under the assumption that $\alpha^2 F = F_{\text{Mo}}$. The apparent T^2 behavior of $\rho(T)$ is not recovered, hence this model for $\alpha^2 F$ can clearly be ruled out. In this regard recent isotope-effect-coefficient measurements⁴⁴ on Mo_6Se_8 indicate that modes associated with displacements of Se atoms, and not just Mo atoms, are important in determining T_c . The isotope-effect results on Mo_6Se_8 were also interpreted to indicate that the higher-energy internal-type modes also contribute to $\alpha^2 F$. The following analysis of $\rho(T)$ for PbMo_6S_8 supports this contention: use of a model $\alpha^2 F$ that contains only the (external-type) modes below 18 meV yielded a $\rho(T)$ which was found to deviate negatively from an apparent T^2 behavior above 30 °K. Hence, such a model is not in accord with experiment. The gross form of $\alpha^2 F$ that is evolving is one that is related to $F(\omega)$ to an extent similar to that found for other superconducting systems. No strong δ -function-type regions seem to be present in $\alpha^2 F$ and controlling T_c . This is in contrast to the early speculation²⁰ that T_c may be governed by torsional and acoustical branches of $F(\omega)$. We have seen that torsional motion is hybridized with internal-type modes (Fig. 8) for PbMo_6S_8 . This should be true to an even greater extent for Mo_6Se_8 . Hence, the degree to which torsional modes contribute to $\alpha^2 F$ is not straightforward to answer. Detailed analyses of the isotope-effect studies may help answer such questions.

IV. SUMMARY OF CONCLUSIONS

These calculations were performed to provide a test and firmer foundation for the molecular-crystal model of the lattice dynamics of Chevrel-phase superconductors. The applicability of the BvK approach using LJ potentials suggests that short-range interactions are important, as

expected within the molecular-crystal model. Hybridization of external acoustical and Pb-atom-dominated optical modes was found to produce interesting structure in the dispersion curves along Λ . Verification of these predicted features await inelastic-neutron-scattering studies on single crystals. Site-weighted frequency moments, densities of states, and Debye temperatures were calculated for representative Chevrel-phase compounds. Torsional-character modes were found where predicted previously using the molecular-crystal model. However, internal-external mode mixing presumably caused the torsional motion to be hybridized with breathing motion within a Mo_6 octahedron for a representative mode studied. Reasonable agreement was found upon comparison of the present calculations with experimental lattice heat capacities and entropies^{7,19,20,31} and generalized phonon densities of states determined by means of inelastic-neutron-scattering studies of polycrystalline samples.^{6,20} We emphasize that the calculations for the compounds other than PbMo_6S_8 should be treated with some caution, since the lattice constant, rhombohedral angle, and the force constants were taken throughout

to be those appropriate to PbMo_6S_8 . The anharmonic temperature dependence of the ^{119}Sn Mössbauer recoil-free fraction^{21,22} in SnMo_6S_8 was not as amenable to the present analysis as the above, possibly due to the multiplicity of available sites straddling the origin²³ as for $\text{Cu}_4\text{Mo}_6\text{S}_8$. The T^2 -resistivity behavior below 40 °K for sputtered films^{34,35} of PbMo_6S_8 could be understood as arising from non-Debye-like structure in $F(\omega)$, as had been demonstrated previously^{36,38} for the A-15 superconductors Nb_3Sn and V_3Si . The temperature dependence of the resistivity below 40 °K was used to determine the plausibility of various models for the superconducting tunneling function α^2F . It was found that modes associated with displacements of chalcogenide as well as Mo atoms, and internal as well as external modes contribute to α^2F and hence λ and T_c .

ACKNOWLEDGMENTS

We would like to thank G. S. Knapp, F. Y. Fradin, and D. J. Lam for their encouragement in the initial stages of this project and T. E. Klippert for a useful discussion. Work supported by the U. S. Department of Energy.

¹R. Chevrel, M. Sergent, and J. Prigent, *J. Solid State Chem.* **3**, 515 (1971).

²R. N. Shelton, in *Superconductivity in d- and f-Band Metals*, edited by D. H. Douglass (Plenum, New York, 1976), p. 137.

³S. Foner, in Ref. 2, p. 161.

⁴Ø. Fischer, M. Decroux, R. Chevrel, and M. Sergent, in Ref. 2, p. 175.

⁵B. P. Schweiss, B. Renker, E. Schneider, and W. Reichardt, in Ref. 2, p. 189.

⁶S. D. Bader, S. K. Sinha and R. N. Shelton, in Ref. 2, p. 209.

⁷F. Y. Fradin, G. S. Knapp, S. D. Bader, G. Cinader, and C. W. Kimball, in Ref. 2, p. 297.

⁸R. W. McCallum, D. C. Johnston, R. N. Shelton, and M. B. Maple, in Ref. 2, p. 625.

⁹M. Marezio, P. D. Dernier, J. P. Remeika, E. Corenzwit, and B. T. Matthias, *Mater. Res. Bull.* **8**, 657 (1973).

¹⁰Ø. Fischer, A. Treyvard, R. Chevrel, and M. Sergent, *Solid State Commun.* **17**, 721 (1975).

¹¹O. Bars, J. GuilleVIC, and D. Grandjean, *J. Solid State Chem.* **6**, 48 (1973).

¹²B. T. Matthias, M. Marezio, E. Corenzwit, A. S. Cooper, and H. E. Barz, *Science* **175**, 1465 (1972).

¹³R. Odermatt, Ø. Fischer, H. Jones, and G. Bongli, *J. Phys. C* **7**, L13 (1974).

¹⁴M. Ishikawa and Ø. Fischer, *Solid State Commun.* **23**, 37 (1977).

¹⁵J. W. Lynn, D. E. Moncton, G. Shirane, W. Thomlinson, J. Eckert, and R. N. Shelton, *J. Appl. Phys.* **49**, 1389 (1978).

¹⁶R. W. McCallum, D. C. Johnston, R. N. Shelton,

W. A. Fertig, and M. B. Maple, *Solid State Commun.* **24**, 501 (1977).

¹⁷L. F. Mattheiss and C. Y. Fong, *Phys. Rev. B* **15**, 1760 (1977).

¹⁸O. K. Andersen, W. Klose, and H. Nohl, *Phys. Rev. B* **17**, 1209 (1978).

¹⁹S. D. Bader, G. S. Knapp, and A. T. Aldred, *Ferroelectrics* **17**, 321 (1977).

²⁰S. D. Bader, G. S. Knapp, S. K. Sinha, P. Schweiss, and B. Renker, *Phys. Rev. Lett.* **37**, 344 (1976).

²¹R. W. Kimball, L. Weber, G. VanLanduyt, F. Y. Fradin, B. D. Dunlap, and G. K. Shenoy, *Phys. Rev. Lett.* **36**, 412 (1976).

²²J. Bolz, J. Hauch, and F. Pobell, *Z. Phys. B* **25**, 351 (1976).

²³K. Yvon, *Solid State Commun.* **25**, 327 (1978), and references therein.

²⁴R. Chevrel, M. Sergent, and Ø. Fischer, *Mater. Res. Bull.* **10**, 1169 (1975).

²⁵H. G. Smith, N. Wakabayashi, and M. Mostoller, in Ref. 2, p. 223.

²⁶Y. Nakagawa and A. D. B. Woods, *Phys. Rev. Lett.* **11**, 271 (1963); R. I. Sharp, *J. Phys. C* **2**, 421 (1969).

²⁷H. G. Smith and W. Gläser, *Phys. Rev. Lett.* **25**, 1611 (1970); H. G. Smith, in *Superconductivity d- and f-Band Metals*, edited by D. H. Douglass (AIP, New York), Vol. 4., p. 321.

²⁸S. K. Sinha and B. N. Harmon, in Ref. 2, p. 269.

²⁹M. Gupta and A. J. Freeman, in Ref. 2, p. 313.

³⁰C. J. Bradley and A. P. Cracknell, in *The Mathematical Theory of Symmetry in Solids* (Clarendon, Oxford, 1972), p. 92.

³¹S. D. Bader and G. S. Knapp (unpublished).

- ³²F. Gompf, H. Lau, W. Reichardt, and J. Salgado, in *Proceedings of the Fifth IAEA Symposium on Neutron Inelastic Scattering* (International Atomic Energy Agency, Vienna, 1972), p. 137.
- ³³A. H. Wilson, Proc. R. Soc. A 167, 580 (1938); A. H. Wilson, *Theory of Metals* (Cambridge U.P., Cambridge, 1954).
- ³⁴J. A. Woollam, S. A. Alterovitz, and H. L. Luo, Bull. Am. Phys. Soc. 22, 402 (1977).
- ³⁵J. A. Woollam and S. A. Alterovitz (unpublished).
- ³⁶G. W. Webb, Z. Fisk, J. J. Engelhardt, and S. D. Bader, Phys. Rev. B 15, 2624 (1977).
- ³⁷V. A. Marchenko, Sov. Phys. Solid State 15, 1261 (1973).
- ³⁸S. D. Bader and F. Y. Fradin, in Ref. 2, p. 567.
- ³⁹R. W. Cohen, G. D. Cody, and J. J. Halloran, Phys. Rev. Lett. 19, 840 (1967), and references therein.
- ⁴⁰Z. Fisk and G. W. Webb, Phys. Rev. Lett. 36, 1084 (1976), and references therein.
- ⁴¹Z. Fisk and A. C. Lawson, Solid State Commun. 13, 277 (1973).
- ⁴²P. B. Allen, J. C. K. Hui, W. E. Pickett, C. M. Varma, and Z. Fisk, Solid State Commun. 18, 1157 (1976); P. B. Allen, Phys. Rev. Lett. 37, 1638 (1976); M. J. Laubitz, C. R. Leavens, and R. Taylor, Phys. Rev. Lett. 39, 225 (1977).
- ⁴³P. B. Allen, Phys. Rev. B 9, 305 (1971), see the Appendix therein.
- ⁴⁴F. J. Culetto and F. Pobell, Phys. Rev. Lett. 40, 1104 (1978).